A Rotation-Lightweight Wireless Power Transfer System for Solar Wing Driving

Kai Song, *Member, IEEE*, Bingqing Ma, Guang Yang, Jinhai Jiang, Ruizhi Wei, Hang Zhang, and Chunbo Zhu, *Member, IEEE*

***Abstract*—In this paper, a novel magnetic coupler of wireless power transfer system for the solar wing driving of the spacecraft is designed. Compared with the traditional slip-ring power supply, the proposed magnetic coupler is characterized by noncontact, high efficiency, wear free, safety, and reliability. Particularly, it can be applied to the rotating condition. To realize light weight and small volume of the receiver, the magnetic coupler has been optimized from both compensation topology and coil configuration. First, a series-none topology is employed to eliminate the bulky secondary-side compensation capacitor. Second, a new nested solenoid coil with strip core is proposed to ensure miniaturization, stable power transfer, and high efficiency. Finally, the experimental setup is built to verify the performance of the designed magnetic coupler. Experimental results are well matched to simulations, demonstrating that the weight of the prototype is 1.3 kg and the transfer power is 3 kW at an ac–dc efficiency of 92.7%.**

***Index Terms*—Rotary magnetic coupler, series-none (S-0) topology, solar wing driving, solenoid coil, strip core, wireless power transfer (WPT).**

I. Introduction

AT PRESENT, satellites and other spacecraft rely mainly on conductive slip rings on the solar wings to supply power for the equipment in the cabin. There are three problems associated with the power transfer method.

1) The large friction of the conductive slip ring causes rapid wear and tear. Local overheating may occur due to the large contact resistance and subsequently cause mechanical deformation. In the long term, wear and tear as well as mechanical deformation will inevitably lead to unreliable contacts, affecting the stability of power transfer.

Manuscript received August 2, 2018; revised October 22, 2018; accepted December 4, 2018. Date of publication December 14, 2018; date of current version June 10, 2019. This work was supported in part by the National Natural Science Foundation of China under Grants 51677032 and 51577034, in part by the Natural Science Foundation of Heilongjiang Province under Grant E2017045, in part by the Harbin Science and Technology Innovation Talents Special Fund Project under Grant 2016RAQXJ002, and in part by the China Postdoctoral Science Foundation under Grants 2014M560254 and 2015T80338. Recommended for publication by Associate Editor U. K. Madawala. *(Corresponding author: Jinhai Jiang.)*

K. Song, G. Yang, J. Jiang, R. Wei, H. Zhang, and C. Zhu are with the School of Electrical Engineering and Automation, Harbin Institute of Technology, Harbin 150001, China (e-mail:

From the above discussion, it is concluded that existing researches on WPT technology in space applications have the following problems.

1) *Low output power:* A series of literatures investigate the design principle of a rotating power transfer system for space applications. However, most prototypes are designed to validate the theory and few high-power models are proposed [13]. Lee *et al.* [14] design and implement a contactless maglev rotating power transfer system with new rotary inductive-coupled structure for the testing equipment on shaft of high-speed rotation applications. Restricted by the dimension and relatively low operating frequency, the output power of the proposed prototype is less than 300 W, which cannot imply problems occur in a high-power design. In [15], a novel ball-joint structure is used for the magnetic coupler. The stable system performance against the displacement angle is highlighted. However, small size leads to low output power and cannot be adopted for spacecraft. In short, small self-inductance and few cores caused by limited dimension reduce the system power capacity and lead to low output power.
2) *Low transmission efficiency:* Low efficiency of current applications is mainly caused by the magnetic and electrical parameters that are not optimized. As for magnetic parameters, Lee *et al.* [14] compared several magnetic couplers with different ferrite cores. However, due to the lack of the tradeoff between the coupling and weight, the coupling coefficient is lower than most applications. Smeets *et al.* [16] propose a rotating transformer based on a pot core geometry. Because of different flux density distribution in magnetic circuit, some parts of the pot core are redundant and a large assumption of core increases core loss. Thus, core structure needs to be optimized to make the flux density uniform and minimize the loss. For electrical parameters, in [16], copper wire is adopted and the number of turns is large. The serious proximity effect and skin effect lead to relatively low efficiency.
3) *High weight:* Most rotary transformers are applied in sealing rollers and space applications which have strict requirements for weight. As discussed before, when the pot core is applied, the weight is intuitively increased compared to others. Therefore, the tradeoff between the coupling and weight needs to be considered. In addition, S-S topology is used in [10] and [17], of which the bulky compensation capacitors increase the weight and complicity of the receiver.

In conclusion, the research gap still exists and needs to be investigated further in this paper.

1) The dimension of the magnetic coupler needs to be optimized for high power density. Most of the rotating couplers proposed in the current research are designed for low-power situation. For high-power applications, the arbitrary size increase is not the choice after optimization. The size and power increase need compromise, which is one of the key points of this paper. Moreover, research on specific problems of high-power applications, such as device stress, heating, and magnetic saturation, is still limited.
2) The rotating coupler for spacecraft is a special application because of its high coupling coefficient and compact structure. Thus, in this paper, the compensation topology that is suitable for high coupling coefficient and relatively small self-inductance will be analyzed. Considering the increasing coil resistance, the number of turns is optimized for the tradeoff between mutual inductance and coil resistance to realize the high efficiency. In addition, appropriate Litz wire also needs to be selected to replace the conventional copper wire in high frequency.
3) To reduce the weight of the rotating coupler, with the magnetic circuit model and flux density distribution, unnecessary core will be eliminated and the core configuration is optimized without reducing power density. For example, conventional pot core is characterized by its high coupling coefficient while large assumption of core and large weight, which is optimized in this paper. Moreover, in this paper, the novel compensation topology will be introduced to reduce electronic components.

Considering the issues of current research, the aim of this paper is to design a magnetic coupler of WPT system with 10-mm air gap and 3-kW power output capability for a lightweight solar wing driving of the spacecraft. With solenoid coil with strip core (SCSC-type) and S-0 topology, the proposed magnetic coupler is lightweight, efficient, reliable, and stable. The remaining of this paper is structured as follows. In Section II, system structure and theoretical analysis are given. Modeling and magnetic field optimization of the proposed SCSC-type coil are performed in Section III. The experimental results are provided in Section IV. The conclusion is presented in Section V.

II. System Structure and Theoretical Analysis

The effects of mutual inductance and load resistance on efficiency and power levels are analyzed using the equivalent model of the resonant circuit. The results are then compared with S-S topology. Based on theoretical analysis and circuit simulation, the required mutual inductance, the secondary self-inductance, and optimal loads for optimizing the transmission efficiency and output power are determined, respectively.

A. System Structure

It is desirable to have a simple structure at the secondary side due to rotating condition. Therefore, an S-0 topology is proposed as the compensation topology of the magnetic coupler. For the S-0 topology, the reflected imaginary impedance from the secondary side is compensated at the primary side. Furthermore, the receiver is greatly simplified without the compensation capacitors. The diagram of the system is shown in Fig. 1.

As shown in Fig. 1, $I_i\ (i = 1, 2)$ are the primary or secondary resonant currents. $L_i\ (i = 1, 2)$ are the self-inductances. $R_i\ (i = 1, 2)$ are the coil internal resistances. R_L is the load resistance.

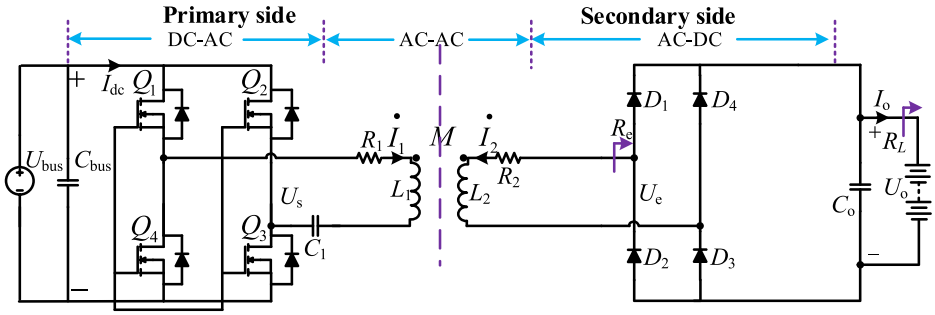

Fig. 1. Circuit model of the designed WPT system.

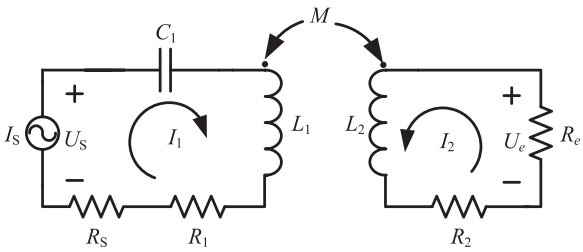

Fig. 2. Equivalent circuit of S-0 topology.

B. Circuit Analysis

The equivalent circuit of S-0 topology is shown in Fig. 2. The inverter is controlled to output constant current I_s, where U_s is the inverter's output voltage, R_s is the equivalent resistance of the inverter, and ω is the operating frequency. The secondary resistance Z_s can be written as

$$Z_S = R_2 + R_e + j\omega L_2. \tag{1}$$

The equivalent load resistance R_e is given by

$$R_e = \frac{8}{\pi^2} R_L. \tag{2}$$

The reflected impedance Z_r from secondary side to primary side is expressed as

$$Z_r = \frac{\omega^2 M^2}{R_2 + R_e + j\omega L_2}. \tag{3}$$

Combined with Z_r, the primary-side impedance is given by

$$Z_p = R_1 + R_s + j\omega L_1 + \frac{1}{j\omega C_1} + \frac{\omega^2 M^2}{R_2 + R_e + j\omega L_2}. \tag{4}$$

The resonance capacitor C_1 can be obtained by (5), while Z_p is purely resistive, namely

$$\mathrm{Im}\,(Z_p) = j\omega L_1 + \frac{1}{j\omega C_1} - \frac{j\omega^3 M^2 L_2}{(R_2 + R_e)^2 + \omega^2 L_2^2} = 0. \tag{5}$$

Furthermore, C_1 is deduced as

$$C_1 = \frac{(R_2 + R_e)^2 + \omega^2 L_2^2}{\omega^2 L_1 (R_2 + R_e)^2 + \omega^4 L_1 L_2^2 - \omega^4 M^2 L_2}. \tag{6}$$

Combined with (6), the real part of Z_p can be given

$$\mathrm{Re}\,(Z_p) = R_1 + R_s + \frac{\omega^2 M^2 (R_2 + R_e)}{(R_2 + R_e)^2 + \omega^2 L_2^2}. \tag{7}$$

According to the Kirchhoff's voltage law, the system is described as

$$\begin{cases} \left(R_1 + R_s + j\omega L_1 + \dfrac{1}{j\omega C_1}\right)\dot{I}_1 + j\omega M \dot{I}_2 = \dot{U}_s \\ j\omega M \dot{I}_1 + (R_2 + R_e + j\omega L_2)\dot{I}_2 = 0. \end{cases} \tag{8}$$

The secondary resonant current $\dot{I}_2$ is deduced as

$$\dot{I}_2 = \frac{j\omega M \dot{I}_1}{R_2 + R_e + j\omega L_2}. \tag{9}$$

Therefore, the system input and output powers are calculated by

$$P_{\substack{\mathrm{in} \\ s-0}} = \left|\dot{I}_1\right|^2 \mathrm{Re}\,(Z_p) = I_1^2 \left(R_1 + R_s + \frac{\omega^2 M^2 (R_2 + R_e)}{(R_2 + R_e)^2 + \omega^2 L_2^2}\right) \tag{10}$$

$$P_{\substack{\mathrm{out} \\ s-0}} = \left|\dot{I}_2\right|^2 R_e = \frac{I_1^2 \omega^2 M^2 R_e}{(R_2 + R_e)^2 + \omega^2 L_2^2}. \tag{11}$$

Through the derivation of (11), the load that ensures the maximum output power is expressed as

$$R_{\substack{p_{\mathrm{out}}\mathrm{max} \\ s-0}} = \sqrt{R_2^2 + \omega^2 L_2^2}. \tag{12}$$

The maximum output power of S-0 topology can be expressed as

$$\begin{aligned} P_{\substack{\mathrm{out\_max} \\ s-0}} &= \frac{I_1^2 \omega^2 M^2 \sqrt{R_2^2 + \omega^2 L_2^2}}{\left(R_2 + \sqrt{R_2^2 + \omega^2 L_2^2}\right)^2 + \omega^2 L_2^2} \\ &= \frac{I_1^2 k^2 Q^2 (R_1 + R_s)\sqrt{(1 + Q_2^2)}}{\left(1 + \sqrt{(1 + Q_2^2)}\right)^2 + Q_2^2} \end{aligned} \tag{13}$$

where k is the coupling coefficient, Q is the quality factor of the coils, and Q_i $(i = 1, 2)$ denote primary or secondary sides, respectively, $Q = \sqrt{Q_1 Q_2}$, $Q_1 = \frac{\omega L_1}{R_1 + R_S}$, and $Q_2 = \frac{\omega L_2}{R_2}$.

The coil–coil efficiency is given by

$$\underset{s-0}{\eta} = \frac{\omega^2 M^2 R_e}{(R_1+R_s)\left[(R_2+R_e)^2+\omega^2 L_2^2\right]+\omega^2 M^2 (R_2+R_e)}. \tag{14}$$

Through the derivation of (14), the load that ensures the maximum efficiency is calculated as

$$\underset{s-0}{R_{\eta\_\max}} = \sqrt{R_2^2+\omega^2 L_2^2+\frac{\omega^2 M^2 R_2}{R_1+R_s}} \tag{15}$$

Therefore, the maximum coil–coil efficiency of S-0 topology is deduced as (16) as shown at the bottom of this page.

It is obvious that the maximum output power point is not the same as the maximum transmission efficiency point.

For comparison, the features of S-S topology are also analyzed, and the primary-side equivalent input impedance of S-S topology is given by

$$\underset{s-s}{Z_{\text{in}}} = R_1+R_s+\frac{\omega^2 M^2}{R_2+R_e}. \tag{17}$$

The output power, input power, and efficiency are, respectively, expressed as

$$\underset{s-s}{P_{\text{out}}} = \left|\dot{I}_2\right|^2 R_e = \frac{I_1^2\omega^2 M^2 R_e}{(R_2+R_e)^2} \tag{18}$$

$$\underset{s-s}{P_{\text{in}}} = \left|\dot{I}_1\right|^2 \text{Re}(Z_{\text{in}}) = I_1^2\frac{(R_1+R_S)(R_2+R_e)+\omega^2 M^2}{R_2+R_e} \tag{19}$$

$$\underset{s-s}{\eta} = \frac{\omega^2 M^2 R_e}{(R_1+R_S)(R_2+R_e)^2+\omega^2 M^2(R_2+R_e)}. \tag{20}$$

Through taking the partial derivative, the maximum output power and efficiency of S-S topology are calculated as

$$\underset{s-0}{R_{p_{\text{out}}\_\max}} = \sqrt{R_2^2+\omega^2 L_2^2} \tag{21}$$

$$\underset{s-0}{R_{p_{out}\_\max}} = \sqrt{R_2^2+\omega^2 L_2^2} \tag{22}$$

where the optimal loads are given by

$$\begin{aligned}\underset{s-s}{P_{\text{out}\_\max}} &= \frac{I_1^2(R_1+R_S)\omega^2 M^2}{2(\omega^2 M^2+2(R_1+R_S)R_2))^2} \\ &= \frac{I_1^2 k^2 Q^2}{2R_2(k^2Q^2+2)^2}\end{aligned} \tag{23}$$

$$\begin{aligned}\underset{s-s}{\eta_{\max}} &= \frac{\frac{(\omega M)^2}{(R_1+R_S)R_2}}{\left(1+\sqrt{1+\frac{(\omega M)^2}{(R_1+R_S)R_2}}\right)^2} \\ &= \frac{k^2Q^2}{\left(1+\sqrt{1+k^2Q^2}\right)^2}.\end{aligned} \tag{24}$$

From the derived formula, it can be seen that the efficiency is affected by multiple parameters in S-0 topology. Besides the mutual inductance *M* and the equivalent load R_e, the secondary self-inductance L_2 also needs to be optimized in the proposed S-0 topology. Note that L_2 satisfies the following relationship:

$$M = k\sqrt{L_1 L_2}. \tag{25}$$

Since the two parameters *M* and L_2 are mutually dependent on each other, the effects of *M* and L_2 on efficiency are considered together during the following coil design.

C. Influence of Mutual Inductance

First, the internal resistance of the primary coil and the secondary coil is assumed as 0.1 Ω to simplify the analysis in simulation. The inverter is modeled as a constant current source I_1 and is set as 17 A, and the operating frequency is 85 kHz. Based on the experience, the mutual inductance is selected in the range of 10–80 μH. The secondary self-inductance associated with the mutual inductance range is assumed to be 20, 40, 60, and 80 μH, respectively. The load is adopted as 10, 20, 30, 40, 50, and 60 Ω, respectively. The efficiency curves with respect to the mutual inductance variations of S-0 topology are shown in Fig. 3.

By observing the efficiency curves, it can be concluded that the efficiency of different secondary coils increases with mutual inductance, which is consistent with S-S topology [18]. As the mutual inductance approaches 50 μH, the increase in efficiency with respect to the increase in mutual inductance becomes saturated. For different secondary coils, the efficiency curves differ in values, but the overall trends are consistent. Therefore, the mutual inductance of 50 μH is considered.

Next, it can be observed that the output power is affected by the primary resonant current by referring to (11). The power requirement can be met by adjusting the magnitude of a primary

$$\begin{aligned}\underset{s-0}{\eta_{\max}} &= \frac{\omega^2 M^2\sqrt{R_2^2+\omega^2 L_2^2+\frac{\omega^2 M^2 R_2}{R_1+R_s}}}{2\left(R_2^2+\omega^2 L_2^2\right)(R_1+R_s)+2\omega^2 M^2 R_2+\left(\omega^2 M^2+2R_2(R_1+R_s)\right)\sqrt{R_2^2+\omega^2 L_2^2+\frac{\omega^2 M^2 R_2}{R_1+R_s}}} \\ &= \frac{k^2Q^2}{2\sqrt{(1+Q_2^2+k^2Q^2)}+k^2Q^2+1}\end{aligned} \tag{16}$$

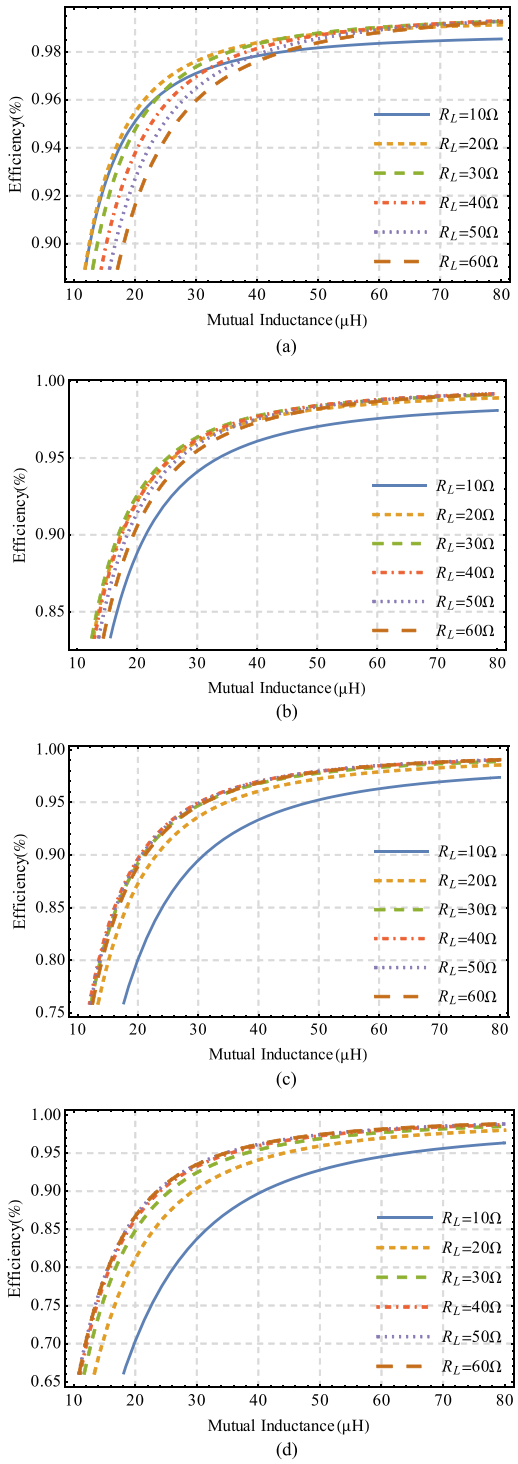

Fig. 3. Efficiency versus mutual inductance at different loads. (a) Secondary self-inductance is 20 μH. (b) Secondary self-inductance is 40 μH. (c) Secondary self-inductance is 60 μH. (d) Secondary self-inductance is 80 μH.

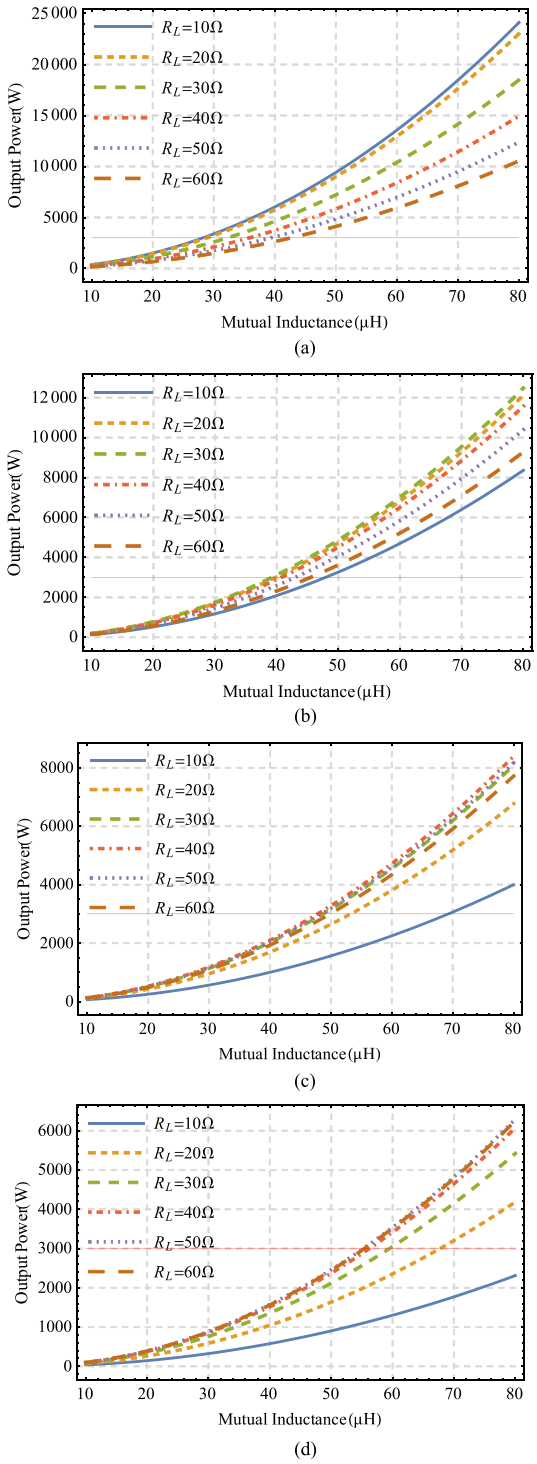

Fig. 4. Output power versus mutual inductance at different loads. (a) Secondary self-inductance is 20 μH. (b) Secondary self-inductance is 40 μH. (c) Secondary self-inductance is 60 μH. (d) Secondary self-inductance is 80 μH.

resonant current. Fig. 4 shows the variations of output power under different loads and different mutual inductance when the primary resonant current is 17 A. The red line indicates 3-kW output power. The crossover points between the red line and the six output power curves show the minimum required mutual inductance for different loads. From observation, it is noted that the output power levels of S-0 topology meet the requirement under all loads when the mutual inductance is 50 μH.

D. *Influence of a Secondary Self-Inductance*

It is necessary to analyze the influence of the secondary self-inductance on the efficiency of S-0 topology. The mutual

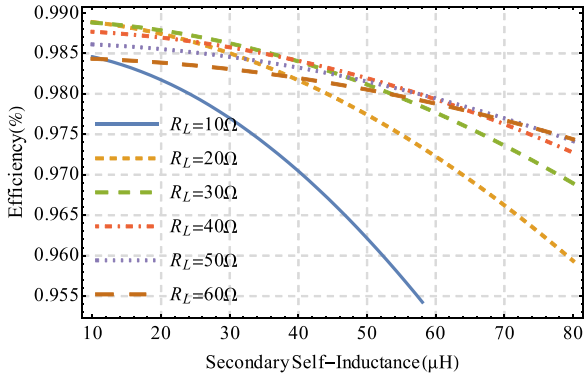

Fig. 5. Efficiency versus secondary self-inductance under different loads.

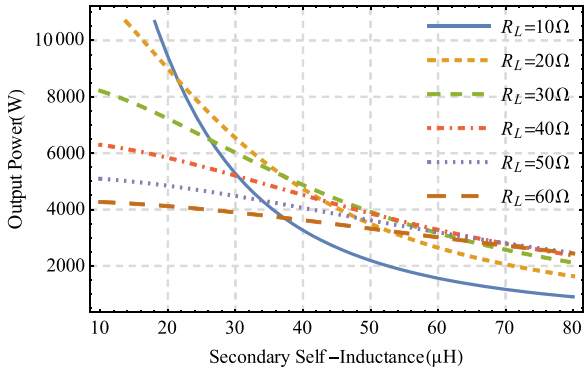

Fig. 6. Output power versus secondary self-inductance at different loads.

inductance is assumed as 50 μH and the load is set as 10, 20, 30, 40, 50, 60 Ω, respectively. Then, the transmission efficiency is calculated when secondary self-inductance varies, as shown in Fig. 5.

It is known from Fig. 5 that the efficiency of S-0 topology is decreased with the increase of the secondary self-inductance, but the decreasing trend of the efficiency becomes slower as the load resistance becomes larger. The effect of L_2 on efficiency is small. The difference between maximum efficiency (L_2 = 10 μH and $R_L = 30\,\Omega$) and minimum efficiency ($L_2 = 60$ μH and $R_L = 10\,\Omega$) is only 3%. When L_2 is reduced, the effect on efficiency can be ignored approximately. Therefore, it can be concluded that:

1) When the mutual inductance is confirmed, the lower the secondary self-inductance is, the higher the efficiency is. The larger the load, the less the efficiency is affected by the secondary coil.
2) From the perspective of efficiency, S-0 topology is more suitable for larger load. However, the output power capability of S-0 topology also needs to be considered.
3) The self-inductance cannot be reduced infinitely. It needs to meet the required mutual inductance. The lower L_2 will lead to a higher L_1 and increase the volume of the primary coil.

The variation of output power versus the secondary self-inductance is shown in Fig. 6. When the secondary self-inductance is relatively small, the output power decreases with the increase of the load. The output power is higher than 3 kW when the value of L_2 is below 60 μH, and it will not output 3 kW when the value of L_2 is larger than 60 μH. Therefore, the secondary self-inductance cannot exceed 60 μH in order to meet the practical power need.

From Figs. 5 and 6, it seems that smaller secondary self-inductance gives higher output power and efficiency. However, L_2 cannot be reduced infinitely. According to (25), the lower L_2 will lead to a higher L_1 after M and k are confirmed. Obviously, to meet the requirement of the mutual inductance, it is necessary to increase L_1 by increasing the number of windings or the outer diameter of L_1 when the value of L_2 is small. This will undoubtedly further increase the volume of the primary coil since the dimension of the magnetic coupler is determined by the largest one in the primary and secondary coils. Therefore, the secondary self-inductance of S-0 topology is selected as 60 μH.

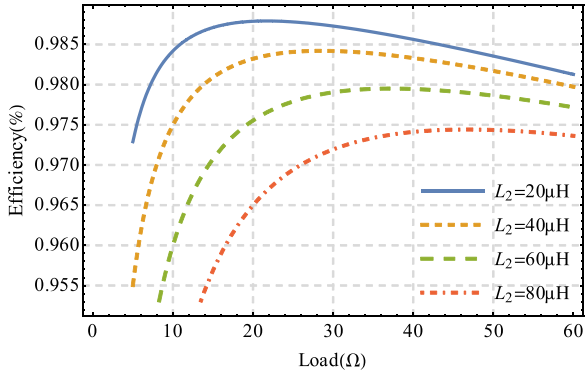

Fig. 7. Efficiency versus load at different self-inductance.

E. Influence of Load

The influence of the load on the efficiency is analyzed in order to obtain the load that ensures the maximum transmission efficiency of S-0 topology. The required output power of the WPT system is 3 kW, the load resistance ranges from 20 to 60 Ω, and the required load-side dc bus voltage is 400 V in this paper.

Fig. 7 shows the efficiency curves with respect to the load variation when the secondary coils have self-inductance of 20, 40, 60, and 80 μH, respectively. It can be found that when the load changes, a peak exists in efficiency, and the corresponding load is the optimal load. The efficiency decreases with the increase of L_2, but the optimal load resistance increases with the increase of L_2. Thus, the optimum load of S-0 topology can be determined after L_2 is determined. In this paper, the mutual inductance is set as 54.0 μH, and the secondary self-inductance is 60.9 μH. Then, the efficiency and output power are plotted under different loads.

From Fig. 8, it can be seen that the maximum efficiency of S-0 topology is around 98.2%, and the corresponding load is 50 Ω. In Fig. 9, the output power curves are plotted against the load when mutual inductance and secondary self-inductance are fixed. The red line in Fig. 9 represents the 3-kW output power. When the primary resonant current is 17 A, the output power

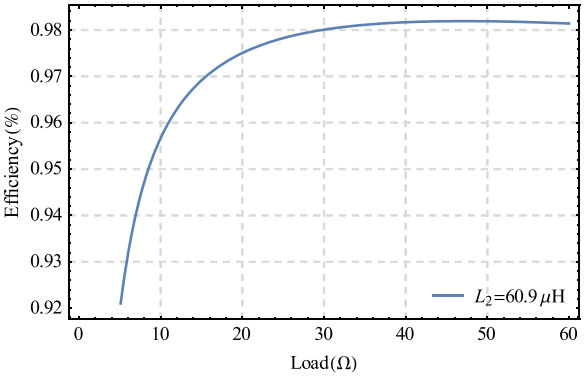

Fig. 8. Efficiency versus load.

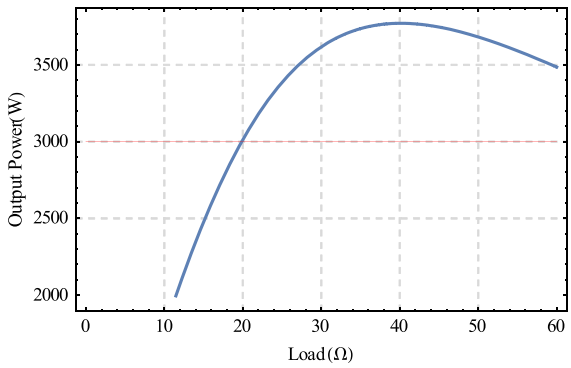

Fig. 9. Output power versus load.

of S-0 topology meets the requirements for load range from 20 to 60 Ω. As can be seen in Figs. 8 and 9, the optimal load that ensures the maximum efficiency is 50 Ω, while the load that ensures the maximum output power is 40 Ω. In the actual design work, we need to maximize the efficiency when power is met. For the wireless powering of the solar wing driving, the requirement of the output power is up to 3 kW, and the maximum power output is not pursued under the experimental parameters. Therefore, for the S-0 topology, in order to achieve the maximum efficiency of the system, 50 Ω is selected as the actual load, which is consistent with the theoretical analysis results.

F. Comparison of Different Topologies

In this section, the proposed S-0 topologies are compared with the S-S topology. From (16) and (20), the denominator of the efficiency $\underset{s-0}{\eta}$ of S-0 topology has an addition expression $(R_1 + R_s)\omega^2 L_2^2$. Therefore, the efficiency of S-0 topology is lower compared to S-S topology. The efficiency of the two topologies is equal only when the secondary self-inductance is close to zero

$$\lim_{L_2 \to 0} \underset{s-0}{\eta} = \lim_{L_2 \to 0} \frac{\omega^2 M^2 R_e}{(R_1 + R_s)\left[(R_2 + R_e)^2 + \omega^2 L_2^2\right] + \omega^2 M^2 (R_2 + R_e)} = \underset{s-s}{\eta}. \tag{26}$$

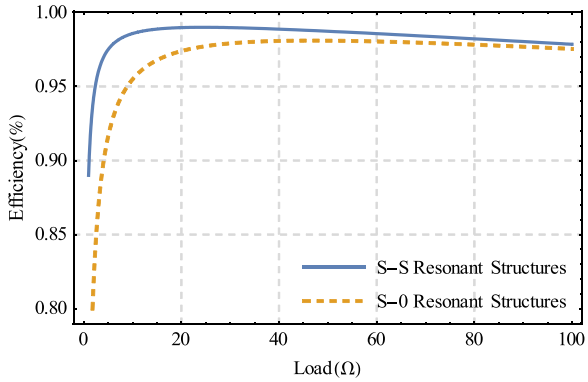

Fig. 10. Efficiency versus load under different topologies.

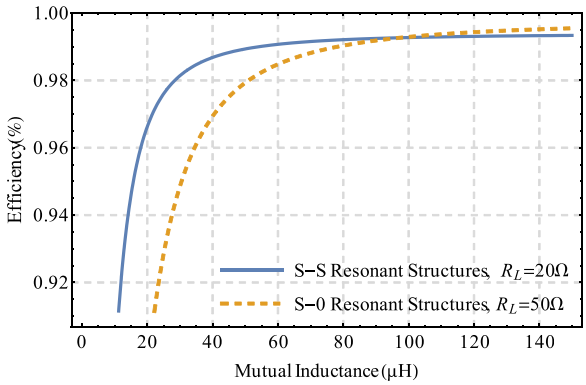

Fig. 11. Efficiency versus mutual inductance under different topologies.

Efficiency curves of the two topologies under different load are plotted in Fig. 10. From the graph, both S-S topology and S-0 topology have a peak efficiency point. The optimal load of S-S topology is 20 Ω, while the optimal load of S-0 topology is 50 Ω. The S-0 topology has lower efficiency than the S-S topology, but as the load increases, the efficiency difference between the two topologies diminishes.

The variation of efficiency with respect to the mutual inductance when both topologies are operating under each optimal load is shown in Fig. 11. From the graph, the efficiency of S-S topology is higher than that of S-0 topology when the mutual inductance is less than 100 μH. On the contrary, the efficiency of S-0 topology is higher than that of S-S topology when the mutual inductance is more than 100 μH.

As can be seen from Figs. 10 and 11, S-S topology has more efficient than S-0 topology but the difference between the two topologies is not large, within 2%. As the load resistance or mutual inductance increases, the efficiency difference will become smaller. Since S-0 topology has no bulky resonant capacitors at the secondary side, which greatly reduce the volume and weight of the secondary side, it is easy to realize the lightweight of the system. Therefore, the S-0 topology is employed in this paper.

III. SCSC-Type Coil Design

Considering the particularity of the WPT system for spacecraft, the designed coil needs to work in a rotating state and follows the design principles of miniaturization, lightweight, high

TABLE I
COMPARISON OF DIFFERENT TYPES OF COILS

Type	Pot-Type		Solenoid-Type	
	Model 1	Model 2	Model 3	Model 4
Model	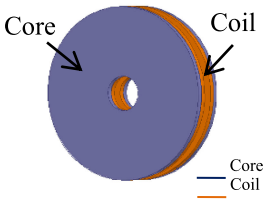	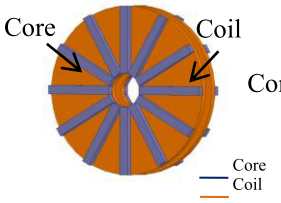	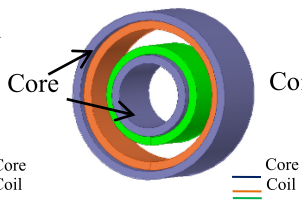	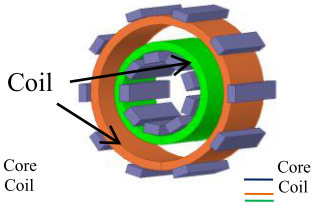
Size/mm	Φ200×30	Φ200×30	Φ100×100	Φ100×100
Air gap/mm	10	10	10	10
k	0.86	0.84	0.91	0.91
Number of turns (N_1: N_2)	18:18	18:18	18:18	18:18
L_1/μH	83.0	68.4	77.7	71.7
L_2/μH	83.0	68.4	74.9	69.5.
M/μH	71.5	57.4	69.6	64.0

Note: the primary coil is orange and the secondary coil is green in Model 3 and 4.

efficiency, and high reliability. Based on the design principles, four different coil models are analyzed, and both of their advantages and disadvantages are compared. Then, the design process is optimized from four aspects with the finite-element analysis (FEA) software Ansoft Maxwell, i.e., with/without core, core bonding direction, dimension of coil, and number of core. Finally, a new SCSC-type coil is designed and the detailed parameters are optimized.

A. Design Criteria

As the core of the whole system, the coil has apparent influence on transmission power and efficiency. The design should meet the following principles.

1) The self-inductance and coupling coefficient of the primary and secondary sides should be given according to the index requirements of the system.
2) The coil should be optimized in accordance with the principle of miniaturization and lightweight, rather than blindly adding cores on the premise of power output capability.
3) The stability of the parameters under rotating condition must be ensured to avoid large fluctuations of transfer power.
4) The magnetic induction intensity in the core should be severely restricted, so as to avoid the magnetic saturation when the transmission power is high.
5) The power losses of the magnetic coupler mainly including losses of the coil and the core should be minimized in the design.
6) Electromagnetic compatibility (EMC) design is employed refer to international standards, such as the International Commission on Non-Ionizing Radiation Protection in order to avoid the interference of strong electromagnetic field.

B. Model Design

According to the actual requirements, the dimension of the coil is limited to 200 × 200 × 200 mm. First of all, two kinds of coils are proposed, which are pot-type and solenoid-type, as shown in Table I.

According to Table I, it can be clearly seen that model 4 is better than the other three models. First, the size is relatively small, which is convenient to installation. Second, the weight and cost are relatively low because of the use of strip core. Moreover, the coupling coefficient is larger than model 1 and model 2, which leads to good coupling performance. Therefore, model 4 namely the SCSC-type is finally determined as the coil model in this paper.

C. With/Without Core

From the perspective of spacecraft application, the principle of lightweight should be followed. Here, the design parameters such as coupling coefficient, self-inductance, and mutual inductance of the primary and secondary coils are compared and analyzed. The simulation results are shown in Table II.

It can be concluded by analyzing the simulation results.

1) The coil without core on both of primary and secondary sides makes the coupler simple and lighter in weight. However, the problem is that coupling performance is decreased sharply, and the mutual inductance cannot be satisfied.

TABLE II
COMPARISON OF DIFFERENT CORES EFFECT

Type	Model 1	Model 2	Model 3	Model 4
Model	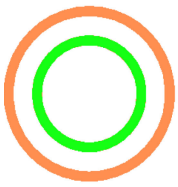	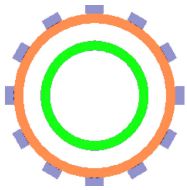	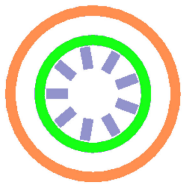	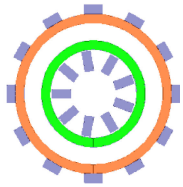
k	0.582	0.608	0.831	0.865
L_1/μH	22.0	26.2	47.0	66.4
L_2/μH	10.4	11.0	50.0	61.9
M/μH	8.8	10.4	40.2	55.4

2) The lack of core on secondary side leads to significant reduction in coupling coefficient and in self-inductance of primary and secondary coils, which is difficult to meet the mutual inductance requirement.
3) The primary coil without core reduces coupling coefficient and self-inductance of the primary and secondary coils to a certain extent, which needs to be compensated by increasing the number of turns. This increases the internal resistance of the coil. Compared with the primary and secondary coils with core, the quality factor Q of the coil is decreased, which leads to the decrease of transmission power and efficiency.
4) From the perspective of EMC, the primary side with core is capable of constraining the magnetic field.

Based on the above analysis, the primary- and secondary-side coils with strip distribution core (model 4) are employed in this paper. Furthermore, it is necessary to optimize the bonding direction, dimension, and number of the core.

D. Bonding Direction

For the SCSC-type coil, the bonding direction of the strip core is further optimized. The different bonding directions of four models are compared, respectively. The simulation results are shown in Table III.

From Table III, it can be known that the coupling coefficient of the four different core bonding modes are approximately the same. The dimension of the coil is increased when the narrow-surface bonding mode is used on the primary side, so the primary-side core with the wide-surface bonding mode is preferred. For the bonding modes of secondary-side core, it shows that the wide-surface bonding mode is slightly better than the narrow-surface bonding mode, for example, the self-inductance and mutual inductance are larger. However, the design of the narrow-surface bonding mode is more conducive to the dimension reduction, so the primary-side core with the wide-surface bonding mode and the secondary side core with the narrow-side bonding mode (model 4) are finally utilized.

E. Coil Dimension

The dimension of the coil is optimized as follows. The air gap is maintained at 10 mm, and the coupling coefficient is simulated when the dimension is changed. The primary and secondary self-inductances, mutual inductance, and flux density distribution are shown in Table IV.

The dimension is expressed as $\Phi D \times L$, where D is the diameter and L is the axial length. From Table IV, it can be seen that when the air gap is constant, the larger the dimension is, the greater the coupling coefficient is and the greater the self-inductance and the mutual inductance are. However, the smaller the size, the easier the magnetic saturation.

The smallest dimension of coil is expected when the mutual inductance satisfies the requirement, meanwhile magnetic saturation does not occur. The upper limit of the magnetic flux density is set to 0.24 T in Table IV. If the dimension exceeds $\Phi 100 \times 80$ mm, magnetic saturation occurs because the number of core is too small. Otherwise, the failure of support frame installation happens because the number of core is too large. Therefore, $\Phi 100 \times 80$ mm is adopted as coil dimension in this paper.

F. Core Number

The optimization is carried out for the number of the primary and secondary cores, where the flux density in the core serves as an important reference. In this paper, PC95 ferrite core of TDK Company is selected. The saturation flux of PC95 ferrite core is 0.4 T. The upper limit of the flux density is set to 0.24 T in Table V. According to the simulation results in Table V, the following conclusions are obtained.

1) Magnetic saturation will occur while the number of the secondary-side core decreases to 8 or less. The coupling coefficient is slightly different, and the self-inductance and mutual inductance of the primary and secondary coils are mildly different when nine or ten pieces of core are used on the secondary side. To lower the weight, nine

TABLE III
EFFECT OF DIFFERENT BONDING DIRECTION

Type	Model 1	Model 2	Model 3	Model 4
Model	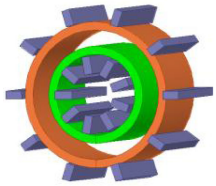	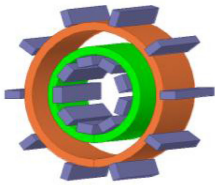	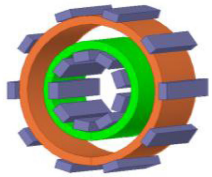	
k	0.9	0.9	0.9	0.9
L_1/μH	67.0	70.4	71.7	70.4
L_2/μH	64.9	69.1	69.5.	67.8
M/μH	59.3	63.1	64.0	62.4

TABLE IV
COMPARISON OF DIFFERENT DIMENSIONS OF COILS

Type	Model 1	Model 2	Model 3	Model 4
Model	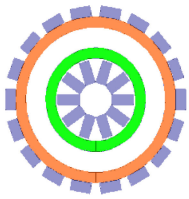	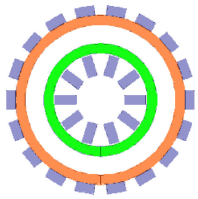	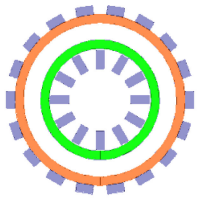	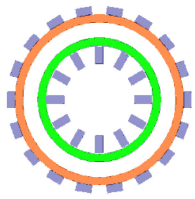
Flux density	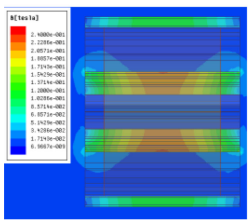	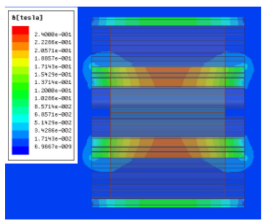	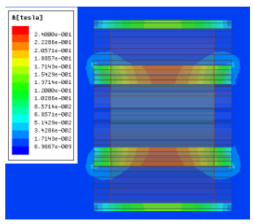	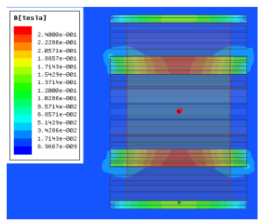
Dimension/mm	Φ90×80	Φ100×80	Φ110×80	Φ120×80
k	0.867	0.869	0.873	0.873
Turns (N_1:N_2)	19:18	18:18	16:15	15:15
L_1/μH	65.3	68.6	63.7	63.0
L_2/μH	54.1	63.8	52.7	58.5
M/μH	51.6	57.6	50.6	51.7

pieces of core are selected on the secondary side in this paper.

2) It can be known that the primary-side core has a little influence on the mutual inductance and magnetic saturation. Therefore, the number of the primary-side core can be determined based on the simulation results of flux density. Meanwhile, it has effect on magnetic field shielding due to the constraint of magnetic field. Through simulation results, it is found that when the number of the primary-side core is chosen as 10, the coil reaches optimal.

Above all, the SCSC-type coil is proposed and the parameters are optimized as below: Ten pieces of core are used on the primary side, while nine pieces for the secondary side, of which are equally spaced.

IV. EXPERIMENTAL EVALUATION

To verify the theoretical analysis and the design criteria, the laboratory level experimental setup is built. It should be noted that the prototype is only a demonstration device to verify the feasibility of the proposed magnetic coupler.

TABLE V
EFFECT OF CORE NUMBER

Type	Model 1	Model 2	Model 3	Model 4	Model 5	Model 6
Model	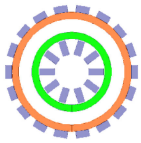	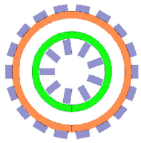	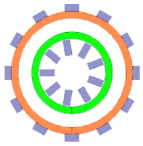	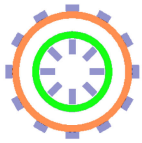	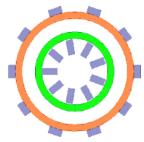	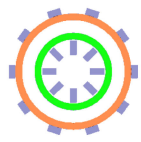
Flux density	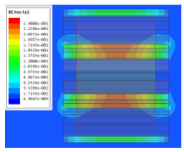	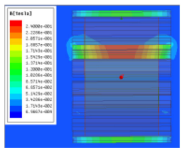	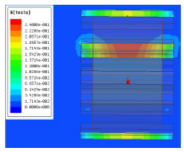	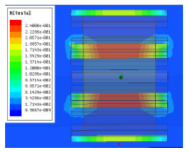	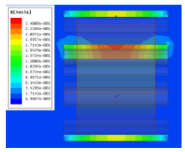	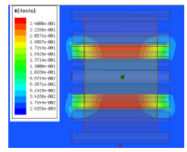
Number of core (P_1:P_2)	18:10	18:9	12:9	12:8	10:9	10:8
k	0.869	0.867	0.865	0.863	0.863	0.861
Turns (N_1:N_2)	17:17	17:17	17:17	18:17	18:18	18:18
L_1/μH	61.2	60.6	59.2	65.1	64.8	63.5
L_2/μH	56.9	56.0	55.2	54.0	60.9	59.6
M/μH	51.4	50.5	49.4	51.1	54.0	53.2

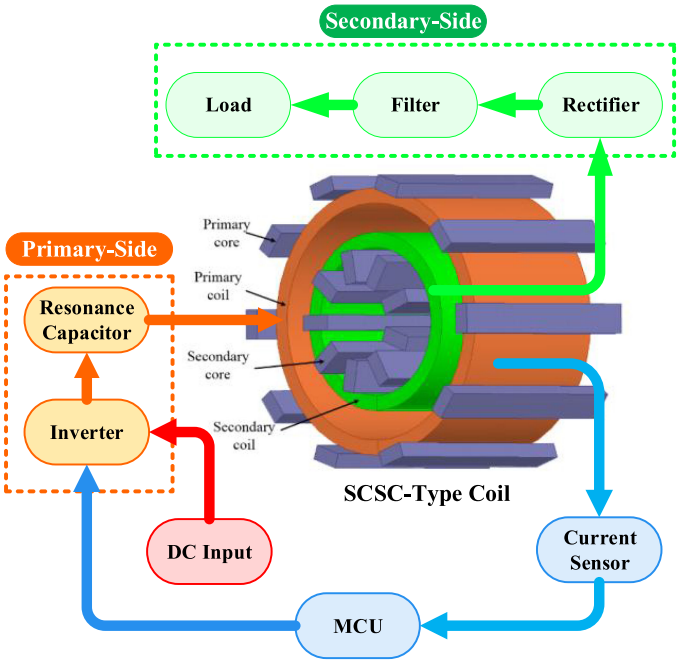

Fig. 12. Structural model of the proposed SCSC-type coil.

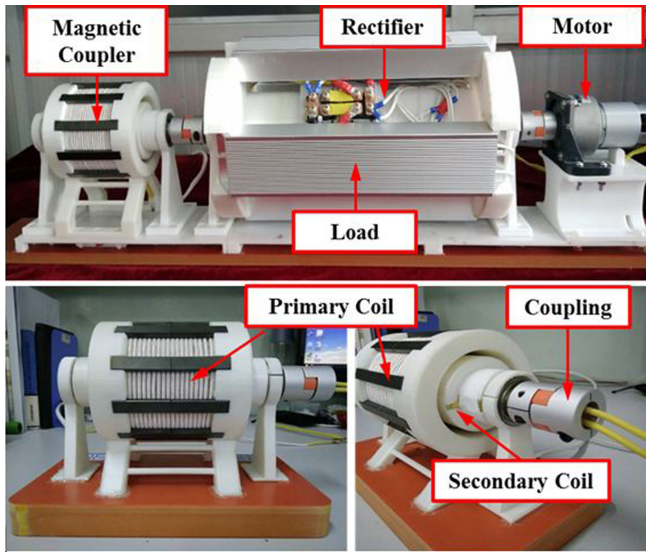

Fig. 13. Prototype system.

A. Prototype System

Based on the above analysis, a SCSC-type coil is proposed, which consists of two nested placed solenoid coils and strip distributed core attached to the coils. The FEA model is shown in Fig. 12. According to the optimization results, a prototype system is built, as shown in Fig. 13. In the system, the core support frame is produced by three-dimensional printing and the 0.1 mm × 500 stranded Litz wire is utilized to wind the coil. The primary coil and core remain stationary, which are fed by the constant current inverter for stable power supply, and the secondary side (including secondary coil, rectifier, and filtering capacitor) is combined with rotating load by the coupling device. The simulation and experimental parameters are shown in Table VI.

It can be seen that the dimension of the rotary lightweight SCSC-type coil is limited to Φ100 × 80 mm and the weight is 1.3 kg, which meets the space application requirement. By using the network analyzer Keysight E5061B, the electrical

TABLE VI
PARAMETERS OF THE PROPOSED SCSC-TYPE COIL

Mechanical	Simulation	Experiment
Dimension: Φ100×80 mm Air gap: 10 mm Single core dimension: 40×10×5 mm Primary core spacing: 36° Primary core spacing: 40° Turns ratio: 18:18 Diameter of Litz wire: 4 mm	Operating frequency: 85 kHz Coupling coefficient: 0.863 Primary self-inductance: 64.8 μH Secondary self-inductance: 60.9 μH Mutual inductance: 54.0 μH	Operating frequency: 82.6 kHz Coupling coefficient: 0.833 Primary self-inductance: 65.4 μH Secondary self-inductance: 60.5 μH Mutual inductance: 52.4 μH Weight: 1.3 kg

parameters of the proposed coil are compared with the simulation results. The experimental coupling coefficient is 0.833 and the mutual inductance is 52.4 μH, which are lower than the simulation results. Meanwhile, the primary and secondary self-inductances are approximately the same as the simulation results. Above all, the designed coil satisfies the demand for mutual inductance in terms of transmission power and efficiency.

B. Stability Verification

As the interval of the primary core is 36°, only by observing the stability of the parameters in the range of 36°, the variation of the parameters in the full range can be inferred. In steps of 4°, the self-inductance, mutual inductance, and coupling coefficient are measured and compared with the simulation results, as shown in Fig. 14.

By observing the changes of mutual inductance, primary/secondary self-inductances, and coupling coefficient, it can be seen that the above parameters of the SCSC-type coil vary smoothly in the rotating state. Therefore, the high stability of the proposed SCSC-type coil is verified, which ensures the constancy of power transmission.

C. Power and Efficiency Measurement

1) Load Variation: In order to verify the correctness of the system design, an experimental study on output power and transmission efficiency (ac–dc, i.e., from inverter's output to load) under different loads is carried out. As shown in Fig. 15, the experimental results are measured by the Power Oscilloscope Yokogawa PX8000 (yellow: inverter's output voltage U_s, green: primary resonant current $I1$, blue: charging voltage U_o, and purple: charging current I_o).

The output power and efficiency are measured when the primary resonant current is 17.2 A and the values of load resistances are 20, 30, 40, 50, and 60 Ω, respectively. The experimental results are compared with the theoretical calculation, as shown in Fig. 16. The results show that the experimental results are slightly lower than calculation because the power losses are ignored during calculation. When the load is 50 Ω, the measured output power is 3.1 kW and the transmission efficiency is 92.7%. At this point, the output voltage is 393.5 V, which satisfies the demand of space application (400-V dc bus voltage). When the load is 40 Ω, the maximum output power is achieved while transmission efficiency is not highest, which illustrates the maximum output power point is not the same as the maximum transmission efficiency point.

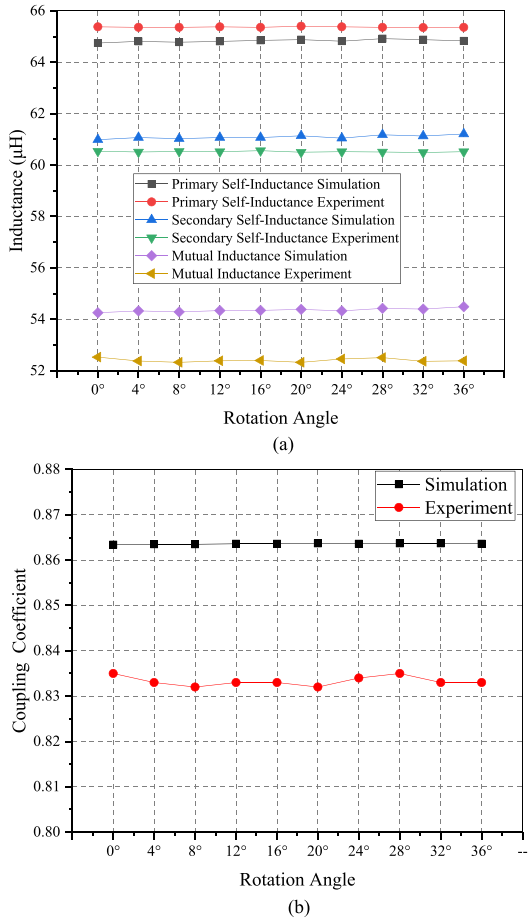

Fig. 14. Variation of parameters in the range of 36°. (a) Self-inductance and mutual inductance versus rotation angle. (b) Coupling coefficient versus rotation angle.

In addition, the measured operating frequency is 82.6 kHz, which is different from the theoretical value of 85 kHz. The main reason is that there are certain errors between the measured values and actual values of resonance capacitors. Meanwhile, the inverter has the function of automatic frequency tracking, which can track the resonance point of the system in real time.

2) Power Measurement: The relationship between different output power and the primary resonant current is analyzed, and then, the experimental results are compared with theoretical calculation, as shown in Fig. 17. It can be seen that the

TABLE VII
PERFORMANCE COMPARISON OF EXISTING ROTARY WPT SYSTEM

Reference	Power/W	Efficiency	Frequency/kHz	Air Gap/mm
[9]@2016	11	58%	125	5
[10]@2014	400	95%	100	8.5
[11]@2016	20	89.7%	520	2
[13]@2014	200	89%	61	--
[14]@2016	297	82%	20	--
[15]@2018	10	81%	585	--
[16]@2010	1000	80%	30	0.5
[17]@2014	1300	95.6%	50	--
This paper	3000	92.7%	85	10

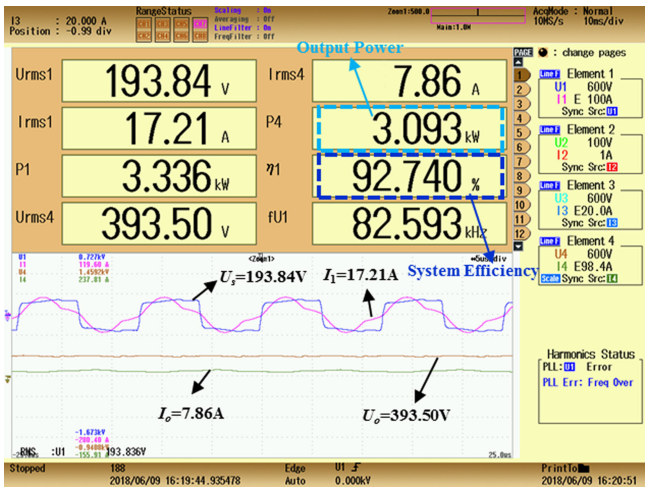

Fig. 15. Experimental waveforms of the proposed magnetic coupler ($RL = 50\ \Omega$).

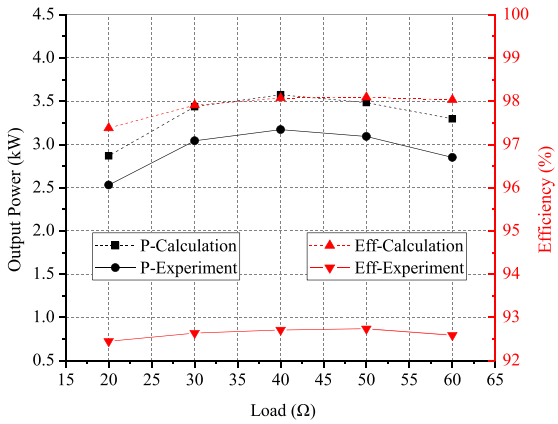

Fig. 16. Output power and transmission efficiency versus load.

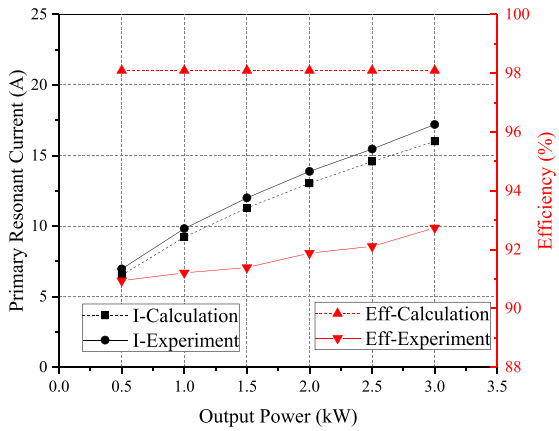

Fig. 17. Primary resonant current and transmission efficiency versus output power.

experimental results are consistent with the calculation results, which demonstrate that the system acquires different output power capacities. If the output power needs to be adjusted, only the primary resonant current needs to be controlled.

When the load is 50 Ω and other experimental conditions are unchanged, the relationship of the experimental efficiency and output power is also shown in Fig. 17. Obviously, under different output power, the experimental efficiency is quite different from the theoretical calculation results. In theory, efficiency does not change with the output power, but, in practice, efficiency increases when the output power increases. The main reason is that the device loss is relatively fixed when the overall power increases, so the efficiency is higher.

3) Rotation Stability: The output power of the system is tested within the scope of the 36°, as shown in Fig. 18. Obviously, the system has good power output stability under rotating condition.

The results also show that the efficiency is almost constant with a little fluctuation. It is proved that the proposed rotary magnetic coupler is characterized by high coupling capability, high power output stability, and high efficiency.

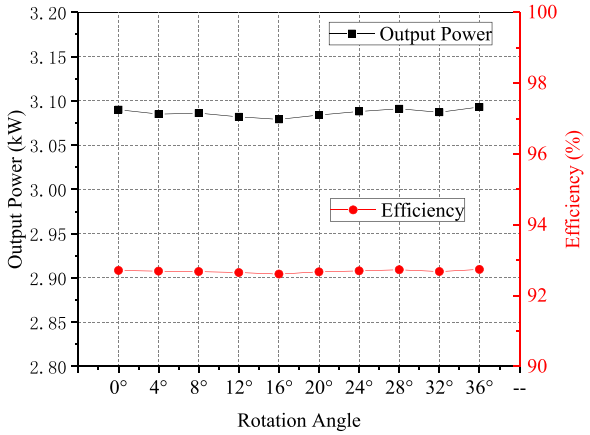

Fig. 18. Output power and efficiency under rotating condition.

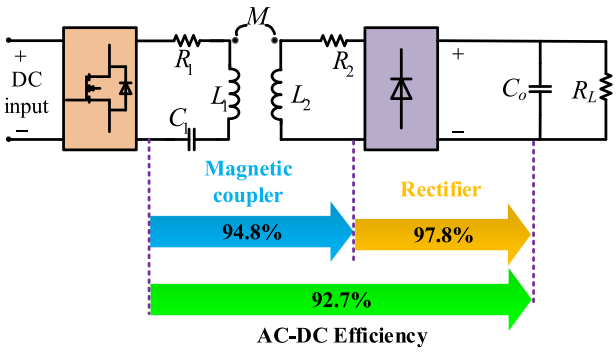

Fig. 19. System efficiency analysis.

D. System Efficiency and Losses Analysis

When the system is measured at the power level of 3 kW, the transmission efficiency is 92.7% (the coil–coil efficiency is 94.5% and the rectifier efficiency is 98.1%), as shown in Fig. 19. The rectifier efficiency is high since the accuracy of the current probe used in the test introduces certain errors.

The total losses of the magnetic coupler are measured to be 173 W and the loss of the rectifier is 71 W. Meanwhile, the loss of the primary and secondary coils is 63 W and the resonance capacitor loss is 59 W. Core loss is calculated to be 51 W since it cannot be directly measured [19]–[22]. Through comparative analysis, the specific proportion of each loss is obtained, as shown in Fig. 20. From the figure, the proportion of rectifier loss is the largest. Among the losses of the magnetic coupler, coil loss accounts for the largest proportion, and the resonance capacitor loss accounts for the lowest proportion.

The designed system in this paper is compared with the existing rotary WPT systems, and the results are shown in Table VII. It can be seen that the existing rotary WPT systems are generally characterized by low-power level, low transmission efficiency, and large weight. The proposed coupler in this paper only weighs 1.3 kg due to the implement of strip core. When air gap reaches 10 mm, the output power is 3.3 kW at an ac–dc efficiency of 92.7%. In summary, the proposed rotation-lightweight coupler shows better performance, which has

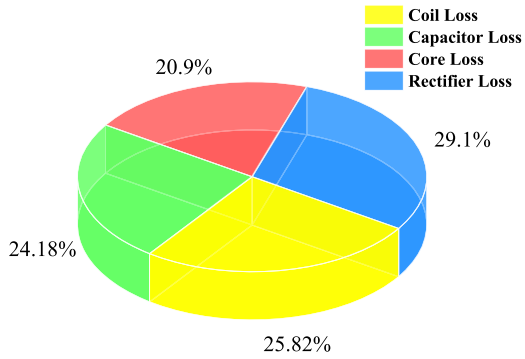

Fig. 20. System loss ratio.

important theoretical significance and practical value in wireless power supply for spacecraft.

V. Conclusion

A novel magnetic coupler of the WPT system for the solar wing driving of the spacecraft is designed in this paper. The coupler consists of nested SCSC-type attached to the coil. The proposed SCSC-type coil enables the magnetic field to be concentrated in the coupler, which ensures strong coupling capability, and, thus, achieves stable and efficient power transmission under rotating condition. Also, multiple pieces of miniaturization strip core are adopted, greatly reducing the core consumption and weight. Furthermore, S-0 resonant topology is proposed to reduce the complexity of the secondary circuit. The dimension and the weight of the magnetic coupler are limited within the $\Phi 100 \times 80$ mm and 1.3 kg, respectively. The experimental results show that the system achieves 3-kW power transmission with 92.7% efficiency at 10-mm air gap, which is suitable for space applications. In practice, the function of information transfer also needs to be involved in the system. Therefore, the next step is to add the information transmission and then realize the synchronous transmission of wireless power and information, which is our later work.

References

[1] L. Zhao, D. J. Thrimawithana, U. K. Madawala, A. P. Hu, and C. C. Mi, "A misalignment tolerant series-hybrid wireless EV charging system with integrated magnetics," *IEEE Trans. Power Electron.*, vol. 34, no. 2, pp. 1276–1285, Feb. 2019.

[2] J. Yin, D. Lin, C. K. Lee, T. Parisini, and S. Hui, "Front-End monitoring of multiple loads in wireless power transfer systems without wireless communication systems," *IEEE Trans. Power Electron.*, vol. 31, no. 3, pp. 2510–2517, Mar. 2016.

[3] J. Miller, O. Onar, and M. Chinthavali, "Primary-Side power flow control of wireless power transfer for electric vehicle charging," *IEEE J. Emerg. Sel. Topics Power Electron.*, vol. 3, no. 1, pp. 147–162, Mar. 2015.

[4] K. E. Koh, T. C. Beh, T. Imura, and Y. Hori, "Impedance matching and power division using impedance inverter for wireless power transfer via magnetic resonant coupling," *IEEE Trans. Ind. Appl.*, vol. 50, no. 3, pp. 2061–2070, Oct. 2013.

[5] G. Buja, M. Bertoluzzo, and K. N. Mude, "Design and experimentation of WPT charger for electric city-car," *IEEE Trans. Ind. Electron.*, vol. 62, no. 62, pp. 7436–7447, Dec. 2015.

[6] G. A. Covic and J. T. Boys, "Modern trends in inductive power transfer for transportation applications," *IEEE J. Emerg. Sel. Topics Power Electron.*, vol. 1, no. 1, pp. 28–41, Jun. 2015.

[7] S. Y. Choi, J. Huh, W. Y. Lee, and C. T. Rim, "Asymmetric coil sets for wireless stationary EV chargers with large lateral tolerance by dominant field analysis," *IEEE Trans. Power Electron.*, vol. 29, no. 12, pp. 6406–6420, Dec. 2014.
[8] S. Li, W. Li, J. Deng, T. D. Nguyen, and C. C. Mi, "A double-sided LCC compensation network and its tuning method for wireless power transfer," *IEEE Trans. Veh. Technol.*, vol. 64, no. 6, pp. 2261–2273, Jun. 2015.
[9] A. Sofia, A. C. Tavilla, R. Gardenghi, D. Nicolis, and I. Stefanini, "Power transfer for rotating medical machine," in *Proc. Annu. Int. Conf. IEEE Eng. Med. Biol. Soc.*, Aug. 2016, pp. 2137–2140.
[10] A. Abdolkhani, A. P. Hu, and N. K. C. Nair, "A double stator through-hole type contactless slipring for rotary wireless power transfer applications," *IEEE Trans. Energy Convers.*, vol. 29, no. 2, pp. 426–434, Jun. 2014.
[11] S. Ditze, A. Endruschat, T. Schriefer, A. Rosskopf, and T. Heckel, "Inductive power transfer system with a rotary transformer for contactless energy transfer on rotating applications," in *Proc. IEEE Int. Symp. Circuits Syst.*, May 2016, pp. 1622–1625.
[12] Y. Zhang, T. Kan, Z. Yan, Y. Mao, Z. Wu, and C. C. Mi, "Modeling and analysis of series-none compensation for wireless power transfer systems with a strong coupling," *IEEE Trans. Power Electron.*, vol. 34, no. 2, pp. 1209–1215, Feb. 2019.
[13] M. Carpita, M. D. Vivo, S. Gavin, and D. Bommottet, "A rotating contactless power transfer system for space applications," in *Proc. IEEE Int. Symp. Power Electron., Elect. Drives, Automat. Motion*, Jun. 2014, pp. 238–242.
[14] J. Y. Lee, L. Y. Huang, and C. Y. Chen, "Design and implementation of contactless maglev rotating power transfer system with new rotary inductive coupled structure," in *Proc. IEEE 8th Int. Power Electron. Motion Control Conf.*, 2016, pp. 2442–2449.
[15] C. Zhang, D. Lin, and S. Y. R. Hui, "Ball-Joint wireless power transfer systems," *IEEE Trans. Power Electron.*, vol. 33, no. 1, pp. 65–72, Jan. 2018.
[16] J. P. C. Smeets, L. Encica, and E. A. Lomonova, "Comparison of winding topologies in a pot core rotating transformer," in *Proc. 12th Int. Conf. Optim. Elect. Electron. Equip.*, 2010, pp. 103–110.
[17] R. Trevisan and A. Costanzo, "A 1-kW contactless energy transfer system based on a rotary transformer for sealing rollers," *IEEE Trans. Ind. Electron.*, vol. 61, no. 11, pp. 6337–6345, Nov. 2014.
[18] K. Song, Z. Li, J. Jiang, and C. Zhu, "Constant current/voltage charging operation for series–series and series–parallel compensated wireless power transfer systems employing primary-side controller," *IEEE Trans. Power Electron.*, vol. 33, no. 9, pp. 8065–8080, Sep. 2018.
[19] Z. Li, K. Song, J. Jiang, and C. Zhu, "Constant current charging and maximum efficiency tracking control scheme for supercapacitor wireless charging," *IEEE Trans. Power Electron.*, vol. 33, no. 10, pp. 9088–9100, Oct. 2018.
[20] J. Hou, Q. Chen, S. C. Wong, C. K. Tse, and X. Ruan, "Analysis and control of series/series-parallel compensated resonant converters for contactless power transfer," *IEEE J. Emerg. Sel. Topics Power Electron.*, vol. 3, no. 1, pp. 124–136, Mar. 2015.
[21] Y. Wang, Y. Yao, X. Liu, D. Xu, and L. Cai, "An LC/S compensation topology and coil design technique for wireless power transfer," *IEEE Trans. Power Electron.*, vol. 33, no. 3, pp. 2007–2025, Mar. 2018.
[22] D. Lin, P. Zhou, W. N. Fu, Z. Badics, and Z. J. Cendes, "A dynamic core loss model for soft ferromagnetic and power ferrite materials in transient finite element analysis," *IEEE Trans. Magn.*, vol. 40, no. 2, pp. 1318–1321, Mar. 2004.

Kai Song (M'12) received the B.S., M.S., and Ph.D. degrees in instrument science and technology from the Harbin Institute of Technology (HIT), Harbin, China, in 2005, 2007, and 2011, respectively.

In 2011, he joined the School of Electrical Engineering and Automation, HIT, as a Lecturer, and was a Visiting Scholar in electrical engineering, The University of Tokyo, Japan, from 2014 to 2015. He has been an Associate Professor with the School of Electrical Engineering and Automation, HIT, since 2016. His current research interests include wireless power transfer, particularly in the high-power wireless power transfer systems for electric vehicles and robots.

Bingqing Ma received the B.S. degree in measurement and control technology and instrument from Yanshan University, Qinhuangdao, China, in 2016, and the M.S. degree in instrument science and technology from the Harbin Institute of Technology, Harbin, China, in 2018.

He is currently with The 54th Research Institute of China Electronics Technology Group Corporation, Shijiazhuang, China. His research interests include wireless power transfer and switching power supply technologies.

Guang Yang received the B.S. degree from the School of Electrical and Information Engineering, Anhui University of Technology, Ma'anshan, China, in 2014, and the M.S. degree from the School of Electrical Engineering and Automation, Harbin Institute of Technology, Harbin, China, in 2017, where he is currently working toward Ph.D. degree.

His research interests include wireless charging technology for electric vehicles.

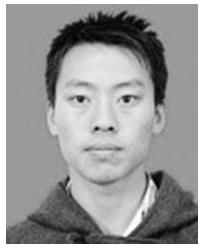

Jinhai Jiang received the B.S. degree from the School of Electronic Science and the M.S. degree from the School of Electrical Engineering and Information from Northeast Petroleum University, Daqing, China, in 2010 and 2013, respectively. He is currently working toward the Ph.D. degree with the Harbin Institute of Technology, Harbin, China.

His research interests include wireless power transfer for supercapacitor and battery-powered online electric vehicles.

Ruizhi Wei received the B.S. degree in information engineering for smart grid from the Nanjing University of Science and Technology, Nanjing, China, in 2018. He is currently working toward the M.S. degree in instrumentation engineering with the Harbin Institute of Technology, Harbin, China.

His research interests include contactless resonant converters and wireless power transfer systems.

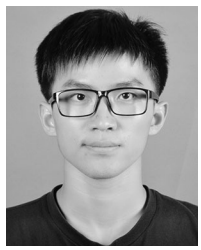

Hang Zhang received the B.S. degree from the School of Control Science and Engineering, Shandong University, Shandong, China, in 2018. He is currently working toward the M.S. degree with the Harbin Institute of Technology, Harbin, China.

His research focuses on wireless power transfer.

Chunbo Zhu (M'05) received the B.S. and M.S. degrees in electrical engineering and the Ph.D. degree in mechanical engineering from the Harbin Institute of Technology (HIT), Harbin, China, in 1987, 1992, and 2001, respectively.

He was a Postdoctoral Research Fellow with the PEI Research Center, National University of Ireland, Galway, Ireland, from 2003 to 2004. He has been a Lecturer with the Department of Automation Measurement and Control, HIT, since 1987. He is currently a Full Professor with HIT, where he leads the Laboratory of Wireless Power Transfer and Battery Management Technologies. His current research interests include energy management systems, electric and hybrid electric vehicles, and wireless power transfer technologies.